Pointing and coverage guarantees for earth-observation satellites via predictive control

Control Engineering Practice 173 (2026) 106979

Contents lists available at ScienceDirect

Control Engineering Practice

journal homepage: www.elsevier.com/locate/conengprac

Pointing and coverage guarantees for earth-observation satellites via predictive control

Martina Mammarella [a,*], Elisa Capello [b], Fabrizio Dabbene [a]

[a] CNR-IEIIT, Turin, Italy
[b] DIMEAS, Politecnico di Torino, Turin, Italy

ARTICLE INFO

Keywords:
Aerospace
Satellite control applications
High accuracy pointing
Model predictive control
Sampling methods

ABSTRACT

Earth-observation satellites require high-accuracy pointing to effectively collect data. This paper introduces a stochastic model predictive control framework that ensures robust pointing and coverage that explicitly accounts for both parametric uncertainty and persistent disturbances. Using offline sampling to approximate chance constraints, it enables real-time onboard implementation. High-fidelity simulations show that the approach reliably achieves pointing and coverage objectives, enhancing autonomy and mission reliability. Moreover, the results show that the stochastic scheme not only outperforms traditional predictive approaches that lack explicit guarantees, but also proves less conservative and computationally demanding than robust predictive methods.

1. Introduction

Satellites specifically designed to observe and study Earth from space play an increasingly important role. Their applications include the study of the environment, the prediction and monitoring of natural disasters, and a more rational exploitation of natural resources. In particular, Earth observation (EO) satellites are used to monitor the Earth's land, ocean, atmosphere, and carbon cycle from space in real-time, and constantly transmit that information to the ground (Zhao et al., 2022). The demand for increased accuracy and efficiency of EO satellites can be effectively supported by the utilization of systems that are highly resilient and autonomous. In this framework, the relevance of pointing accuracy is amplified due to the influence of the attitude control on the on-ground projection of the visibility cone. This aspect is amplified for low Earth orbit (LEO) satellites due to their low altitude and the resulting small footprints (Cakaj et al., 2014).

1.1. Mission context and motivations

To achieve high-resolution imaging of a selected region, the spacecraft must reorient its payload toward the target direction *rapidly* and maintain a tracking status to the target *continuously*. Generally speaking, attaining precise attitude control for imaging or data collection is a significant challenge. Clearly, the relevance of precise attitude control strongly depends on the mission objectives and required pointing accuracy. Indeed, it can range from degrees or fractions of a degree for CubeSat and small satellite missions to arcsecond-level precision for high-end space observatories. Accordingly, novel onboard control systems have to provide *a priori* guarantees of safety and optimized performance, all indices interpretable as constraints, as well as robustness requirements with respect to the changes in employed models and operating conditions.

Among all available control methodologies, model predictive control (MPC) has proven to be one of the most promising in this context, being able to simultaneously address such a broad scope of challenging demands in a systematic manner (see Eren et al. (2017) and references therein). MPC-based approaches are particularly advantageous for attitude reorientation and slewing maneuvers, where state and input constraints, actuator saturation, and transient performance requirements play a critical role. In such scenarios, the ability of MPC to explicitly handle constraints while optimizing transient behavior represents a key benefit over classical control designs. Classical robust control techniques, such as LQG (Pittelkau, 1992) and H_∞ control (Luo et al., 2005), when properly tuned and combined with appropriate guidance (e.g., using feed-forward commands for large-angle maneuvers), can also achieve good performance for trajectory tracking and not only in quasi-steady operating conditions. In the latter case, where disturbance rejection and steady-state performance dominate the control objectives, classical robust controllers remain a natural and effective choice. This work focuses on constrained maneuvering scenarios relevant to Earth-observation missions, rather than on fine pointing operation, and does not pursue a direct comparison with H_∞ or stochastic μ-synthesis approaches. This distinction clarifies the intended operational domain of the proposed stochastic MPC framework and avoids overgeneralization

* Corresponding author.
E-mail addresses: martina.mammarella@cnr.it (M. Mammarella), elisa.capello@polito.it (E. Capello), fabrizio.dabbene@cnr.it (F. Dabbene).

https://doi.org/10.1016/j.conengprac.2026.106979
Received 1 October 2025; Received in revised form 26 March 2026; Accepted 26 March 2026
Available online 2 April 2026

of its applicability. Moreover, while recent learning-based MPC (Koller et al., 2018) and disturbance-observer-enhanced (Hewing et al., 2019) schemes have shown promising results, this work focuses on predictive controllers that provide explicit, offline-verifiable constraint and probabilistic guarantees, which are particularly relevant for safety-critical space applications.

However, MPC schemes may incur relevant performance degradation in the presence of parametric uncertainty (due to, e.g., linearization effects and neglected high-order dynamics) external noise (e.g., sources of environmental disturbance). This may also lead to constraint violation in closed loop and the online optimization being infeasible. To cope with these disadvantages, robust approaches have received significant attention (e.g., Sun et al. (2018)). Such approaches not only guarantee performance under nominal operating conditions, but also ensure satisfactory robustness towards mission and system constraints, including exclusive zone constraints and actuator saturation (see, e.g., Galuppini et al. (2018), Mammarella et al. (2019)).

In the specific case where a stochastic model can be formulated to represent the uncertainty and disturbance, both assumed to be random with known probability distribution, and where some or all the constraints are probabilistic in nature, one can rely on a less conservative class of MPC, namely the stochastic MPC (SMPC). In the optimization framework, constraints involving stochastic parameters that are required to be satisfied with a pre-specified probability threshold are called *chance constraints* (CC). In the space framework, the mathematical form of probabilistic constraints perfectly aligns with the classical form of requirements defined for space systems according to ECSS standards, i.e., "Performance A shall be satisfied with probability X% and confidence level Y%". This correspondence represents a key motivation for proposing a stochastic MPC formulation for the control of pointing error in Earth Observation missions.

In general, dealing with CC implies facing two serious challenges: the solution of difficult parameterized probability integrals and the non-convexity of the ensuing constraints (Geng & Xie, 2019). Consequently, while attractive from a modeling point of view, problems involving CC are often computationally intractable, generally shown to be not solvable in polynomial time, seriously limiting their applicability. With the goal of controlling a fast-dynamics system affected by both parametric uncertainties and additive noise, for real-time implementability it becomes mandatory to reduce the computational cost of the control algorithm. In this case, the class of sample-based approximations have proven to represent valid techniques, especially when involving offline sampling strategies such as in Lorenzen et al. (2017b).

1.2. Main contributions

In this paper, the offline sample-based SMPC (OS-SMPC) approach, first proposed in Mammarella et al. (2018b), is selected to solve the non-trivial problem of extending the results in Lorenzen et al. (2017b) into a comprehensive framework, able to tackle scenarios where both additive noise and parametric uncertainty are simultaneously present. The effectiveness of the so-called OS-SMPC approach was already validated for a rendezvous-like mission profile on an experimental testbed as described in Mammarella et al. (2018b). Here, a nano LEO satellite operating in an Earth observation scenario is considered, and the effectiveness of the controller is assessed during the nadir-pointing operational mode. Specifically, the performance of the OS-SMPC scheme is assessed with respect to the controller update rate and the sample complexity, and its efficiency is further compared with a tube-based MPC scheme in terms of tracking capabilities. Finally, the effect of relaxing constraints on different mission profiles, each one described by a different payload field-of-view (FOV) requirement, is analyzed. In particular, the achievable coverage accuracy is shown to be strictly related to the projected coverage area (which, in turn, is directly related to the payload FOV) and not only to the capability of minimizing the pointing error. The predictive control schemes and their performance in terms of pointing accuracy and coverage have been tested on the high-fidelity *Earth-observation satellite simulator* (EOSS), developed by some of the authors.

The remainder of this paper is organized as follows. Section 2 describes the orbital simulator and the associated reference frames, and dynamical and disturbance models. Section 3 formulates the stochastic predictive control problem, including the sample-based chance constraints, whose probabilistic properties are detailed in Section 4. Simulation results obtained using the EOSS are presented in Section 5, where the OS-SMPC performance is compared with classical and robust schemes in terms of computational time, control effort, and pointing error. Then, the impact of pointing error and payload field-of-view on coverage is analyzed and a novel figure of merit for coverage accuracy is introduced. Conclusions are drawn in Section 6.

Notation. Uppercase letters are used for matrices and lower case for vectors. $[A]_j$ and $[a]_j$ denote the j-th row and entry of the matrix A and vector a, respectively. Positive (semi)definite matrices A are denoted $A \succ 0$ $(A \succeq 0)$ and $\|x\|_A^2 = x^\top A x$. The notation $\mathsf{Pr}\{\mathcal{A}\} = \mathsf{Pr}\{\mathcal{A}|x_k\}$ denotes the conditional probability of an event $\mathcal{A}$ given the realization of x_k, similarly $\mathbb{E}_k\{\mathcal{A}\} = \mathbb{E}\{\mathcal{A}|x_k\}$ for the expected value. We use x_k for the (measured) state at time k and $x_{\ell|k}$ for the state predicted l steps ahead at time k. The sequence of length T of vectors $v_{0|k}, \dots, v_{T|k}$ is denoted by $\mathbf{v}_{T|k}$. The symbol $\otimes$ denotes the tensor (outer) product of two vectors. The subscript $(\cdot)_\oplus$ denotes quantities referenced to the Earth. $\mathbb{I}_n$ is the $n \times n$ identity matrix whereas $\mathbf{1}_m$ is the m column vector of ones. Given $a, b \in \mathbb{N}$, $\mathbb{N}_a^b$ is the set of integers from a to b.

2. Nano-satellite simulator

The EOSS simulator is a high-fidelity MATLAB/Simulink-based tool for Earth observation satellites, validated against NASA's 42 simulator to ensure realistic attitude determination under disturbances. It models orbital and attitude dynamics, environmental disturbances, onboard sensors, and control systems, and it enables visualization of satellite ground tracks and payload coverage based on field of view (Mammarella, 2019).

2.1. Reference frames

In this section, the reference frames later used for describing the satellite motion are briefly recalled.

2.1.1. Earth-centered inertial frame (ECI)

Typically, for describing the orbital motion of a satellite, the geocentric-equatorial system, usually called Earth-centered inertial frame (ECI), is employed. It is fixed with respect to the stars and Earth turns relative to it. This frame has the origin at Earth's center, the X_I-axis points at the vernal equinox, the Z_I-axis points towards the North pole, and the Y_I-axis completes the right-hand triad.

2.1.2. Body frame (b)

The body frame (B) has origin at the instantaneous center-of-mass (moving with mass shifts) and axes parallel to principal structural directions. This ortho-normalized frame yields diagonal inertia tensor and expresses standard Euler equations for attitude, angular velocity, and torque.

2.1.3. Local-vertical/local-horizontal (LVLH)

The reference attitude to be tracked is defined according to the specific scenario. For Earth-observation missions, the reference frame is the so-called local-vertical/local-horizontal (LVLH) frame, centered in the satellite center-of-mass and with axes defined with respect to the ECI frame as follows: i) the Z_L-axis points along the nadir vector towards Earth, i.e., $\hat{k}_L = -r_I/\|r_I\|$; ii) the Y_L-axis points along the orbital angular momentum but in the opposite direction, i.e., $\hat{j}_L = -h_I/\|h_I\|$; and iii) the X_L-axis is in the direction of the orbital velocity, i.e., $\hat{i}_L = \hat{k}_L \times \hat{j}_L$.

2.2. Orbital dynamics

The orbital dynamics in an inertial frame can be described as its relative motion with respect to Earth (Bate et al., 2020) by the two-body equation of motion, i.e.,

$$\ddot{r}_I = -\frac{\mu_\oplus}{\|r_I\|^3} r_I + f_d + f_c,$$

where f_d is the contribution due to the external disturbance sources (see Section 2.4), f_c is the control thrust generated by the main propulsion subsystem, r_I is the Earth-to-spacecraft distance expressed in the inertial frame, and $\mu_\oplus = 398,600\ \text{km}^3/\text{s}^2$ is the Earth's gravitational parameter. If $f_d = f_c = 0$, the satellite trajectory is defined by a conic whose shape depends on the eccentricity e, i.e.,

$$\|r_I\| = \frac{a(1-e^2)}{1+e\cos\nu},$$

where ν is the true anomaly that varies over time as

$$\dot{\nu} = \frac{\sqrt{\mu_\oplus a(1-e^2)}}{\|r_I\|^2}. \tag{1}$$

2.3. Rotational dynamics and kinematics

The spacecraft attitude dynamics is obtained starting from the definition of the rigid-body angular momentum in a non-rotating frame, which leads to Euler's equation (Markley & Crassidis, 2014). This set of equation describe the evolution of the angular velocity ω_{BI} of the satellite body frame with respect to ECI, assuming that the satellite is symmetric and its inertia axes are aligned with the principal axes. Let us consider a spacecraft equipped with reaction wheels or control moment gyros as actuators. Then, the rotational dynamics is given by

$$\dot{\omega}_{BI} = J_{\text{SC}}^{-1}[\tau_B - \omega_{BI} \times (J_{\text{SC}}\omega_{BI} + H_{\text{act}})], \tag{2}$$

in which τ_B is the total external torque acting on the rigid-body, J_{SC} is the spacecraft matrix of inertia, and H_{act} denotes only the angular momentum of the wheels along their spin axes.

The attitude kinematics can be expressed in terms of Euler angles, describing the orientation between the body frame and the reference frame, which in this case is the LVLH (Markley & Crassidis, 2014). Accordingly, the evolution of the Euler angles (ϕ, θ, ψ) (for a 3-2-1 rotation sequence) to the angular velocity of the body frame relative to the reference frame $\omega_{BL} = [\text{p}, \text{q}, \text{r}]^\top$ is related as

$$\begin{aligned}
\dot{\phi} &= \text{p} + \sin(\phi)\tan(\theta)\text{q} + \cos(\phi)\tan(\theta)\text{r},\\
\dot{\theta} &= \cos(\phi)\text{q} - \sin(\phi)\text{r},\\
\dot{\psi} &= \sin(\phi)\sec(\theta)\text{q} + \cos(\phi)\sec(\theta)\cos(\theta)\text{r}.
\end{aligned}$$

Since the Euler angles kinematic model has a singularity for $\theta = 90°$, it is possible to describe the orientation of the satellite with respect to the LVLH frame using a unit quaternion representation $q = [q_1, q_2, q_3, q_S]^\top$, i.e., a four-parameter description of the 3D orientation that avoids singularities, and the kinematics equation becomes

$$\dot{q} = \omega_B \times \text{q} = \frac{1}{2}\Sigma(\text{q})\omega_B, \quad \Sigma(q) = \begin{bmatrix} q_S & -q_3 & q_2 \\ q_3 & q_S & -q_1 \\ -q_2 & q_1 & q_S \\ -q_1 & -q_2 & -q_3 \end{bmatrix}.$$

Remark 1. The attitude dynamics considered in this work rely on a rigid-body spacecraft model. The presence of flexible appendages, such as solar panels or deployable antennas, can be addressed by augmenting the system dynamics with a reduced-order flexible model or by embedding their effects as parametric uncertainty and disturbance terms.

2.4. Disturbance and noise sources

The space environment is the primary source of disturbances acting on the spacecraft, which can jeopardize its dynamics. As external disturbances due to the space environment, four main sources are generally recognized as the primary contributors and have been modeled in EOSS: i) aerodynamic drag ; ii) planetary gravity field; iii) solar radiation pressure (SRP); and iv) spacecraft residual magnetic dipole. It is important to highlight that, instead of the classical cannonball model, an N-plate model has been exploited to approximate the shape of the satellite by a collection of flat plates, each of them representing the different sides of the satellite and having different properties and orientation in the body-fixed frame (Markley & Crassidis, 2014). As discussed in Bate et al. (2020), external disturbances are persistent and may frequently be of the same order of magnitude as the applied torques.

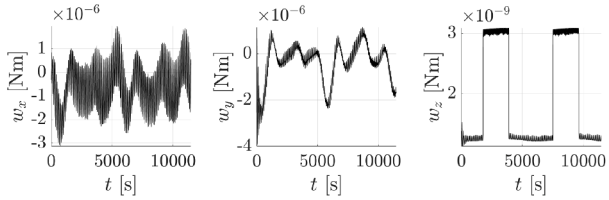

Fig. 1. Evolution over two orbital periods of the total torque due to the environmental disturbance sources.

Fig. 1 illustrates the simulated variation of the total torque over two orbital periods for an elliptical LEO orbit, the same one later considered for the case study.[1] Additionally, EOSS also includes measurement noise sources due to attitude and position sensors equipped on board the selected platform. Specifically, it considers gyroscopes, Sun sensors, magnetometers, and a GPS for positioning tasks (see, e.g., Donati et al. (2023)).

3. Nadir-pointing OS-SMPC control

The satellite dynamics, suitably linearized and discretized[2], can be represented as a discrete-time, linear system

$$x_{k+1} = A(\vartheta_k)x_k + B(\vartheta_k)u_k + Dw_k, \tag{3}$$

affected by both parametric uncertainty ϑ_k and additive noise $w_k \in \mathbb{W}$, with $\mathbb{W}$ a compact and convex set.

Assumption 1 (Bounded Random Disturbance). The disturbances w_k, for $k = 0, 1, 2\ldots$, are independent and identically distributed (iid), zero-mean random variables with support $\mathbb{W}$, which is a bounded and convex set.

Moreover, one can note that the uncertainty ϑ_k also takes into account the linearization errors, modeling inaccuracies, and unmodeled higher-order dynamics. In this case, the system matrices $A(\vartheta_k)$ and $B(\vartheta_k)$ are (possibly nonlinear) functions of the uncertainty ϑ_k under the following assumption on $A(\vartheta_k)$ and $B(\vartheta_k)$.

Assumption 2. The parameters $\vartheta_k \in \Theta \subset \mathbb{R}^{n_\vartheta}$, for $k \in \mathbb{N}$, are realizations of independent and identically distributed (i.i.d.) multivariate real-valued random variables Θ_k. Given $\mathbb{G} = \{(A(\vartheta_k), B(\vartheta_k))\}_{\vartheta_k \in \text{supp}(\Theta_k)}$, its polytopic outer approximation $\bar{\mathbb{G}} = \text{co}\{(A^\imath, B^\imath)_{\imath \in \mathbb{N}_1^{N_c}}\} \supseteq \mathbb{G}$ exists and is known.

Let us consider the state subject to polytopic chance constraints of the form

$$\Pr\left\{[H_x]_j x_{\ell|k} \le [h_x]_j\right\} \ge 1 - \varepsilon, \quad \forall \ell \in \mathbb{N}_{\ge 0},\ j \in \mathbb{N}_1^p, \tag{4}$$

in which the probability of violating state constraint j should not exceed a given violation level probability $\varepsilon \in (0, 1)$. Note that the probability

[1] The specific orbit has a 6924.1 km semi-major axis, a 0.002 eccentricity, a 187.48° inclination, with a 193.5507° RAAN and a 224.7226° argument of periapsis

[2] The dynamics of the satellite has been linearized with respect to the nadir-pointing and nominal orbit, whereas the discretization has been performed using a standard zero-order hold method.

$\Pr\{\cdot\}$ in (4) denotes the joint probability with respect to both the sequences of uncertainty $\boldsymbol{\vartheta}_k \doteq \{\vartheta_{\ell|k}\}_{\ell=0}^{T-1}$ and disturbance $\mathbf{w}_k \doteq \{w_{\ell|k}\}_{\ell=0}^{T-1}$ along the horizon T. Moreover, it is also assumed that the system is subject to hard input constraints, i.e.,

$$H_u u_{\ell|k} \leq 1, \quad \forall \ell \in \mathbb{N}_{\geq 0}. \tag{5}$$

Then, as typical in stabilizing MPC, the analysis relies on the definition of a robust forward invariant set Ameen et al. (2023) to assume the existence of a suitable terminal set $\mathbb{X}_T$ and an asymptotically stabilizing gain K for (3).

Definition 1 (Robust forward invariant set)**.** Let $\mathbb{X} \subset \mathbb{R}^n$ be the state space of (3) where w_k is a bounded disturbance function that takes values in a compact set $\mathbb{W} \subset \mathbb{R}^n$. A set $\mathbb{X}_R \subset \mathbb{S}$ is said to be a robust forward invariant (RFI) set if for any $x \in \mathbb{X}$, one has $x_0 \in \mathbb{X}_R \Rightarrow x_k \in \mathbb{X}_R \, \forall k \geq 0$.

Assumption 3 (Terminal set)**.** There exists a terminal set $\mathbb{X}_T$, which is robustly forward invariant for (3) under the (given) control law $u_k = Kx_k$. Given any $x_k \in \mathbb{X}_T$, the state and input constraints (4)–(5) are satisfied and there exists a matrix $P \in \mathbb{R}^{n\times n}$ such that the following Lyapunov stability, defined for the stochastic linear system $x_{k+1} = A(\vartheta_k)x_k + B(\vartheta_k)u_k$ under state feedback $u_k = Kx_k$, is satisfied, i.e.,

$$Q + K^\top RK + \mathbb{E}\{A_K(\vartheta_k)^\top P A_K(\vartheta_k)\} - P \preceq 0, \tag{6}$$

for all $\vartheta_k \in \Theta$, with $A_K(\vartheta_k) \doteq A(\vartheta_k) + B(\vartheta_k)K$, and with $Q \in \mathbb{R}^{n\times n}$, $Q \succ 0$, $R \in \mathbb{R}^{m\times m}$, $R \succ 0$.

Let us consider the design of a parametrized feedback control law of the form

$$u_{\ell|k} = Kx_{\ell|k} + v_{\ell|k},$$

where K is quadratically stabilizing for the system (3). For a given $x_{0|k} = x_k$, the optimal sequence of correction terms $\mathbf{v}_k$ can be determined by the SMPC algorithm as the minimizer of the *expected* finite-horizon cost

$$J_T(x_k, \mathbf{u}_k) = \mathbb{E}\left\{\sum_{\ell=0}^{T-1}\left(\|x_{\ell|k}\|_Q^2 + \|u_{\ell|k}\|_R^2\right) + \|x_{N|k}\|_P^2\right\}, \tag{7}$$

subject to constraints (4)–(5).

Next, by simple algebraic manipulations, i.e., repeatedly propagating the dynamics from $\ell = 0$, it is possible to derive suitable transfer matrices

$$\Phi^0_{\ell|k}(\boldsymbol{\vartheta}_k) = A_K(\vartheta_{\ell-1|k})A_K(\vartheta_{\ell-2|k})\cdots A_K(\vartheta_{0|k}),$$

$$\Phi^v_{\ell|k}(\boldsymbol{\vartheta}_k) = \begin{bmatrix} A_K(\vartheta_{\ell-1|k})\cdots A_K(\vartheta_{1|k})B(\vartheta_{0|k}) \\ \vdots \\ B(\vartheta_{\ell-1|k}) \\ 0_{n\times(T-\ell)m} \end{bmatrix}^\top,$$

$$\Phi^w_{\ell|k}(\boldsymbol{\vartheta}_k) = \begin{bmatrix} A_K(\vartheta_{\ell-1|k})\cdots A_K(\vartheta_{1|k})\mathbb{I} \\ \vdots \\ \mathbb{I} \\ 0_{n\times(T-\ell)m_w} \end{bmatrix}^\top,$$

$$\Gamma_\ell = [0_{m\times\ell m} \;\; I_m \;\; 0_{m\times(T-\ell-1)m}],$$

such that the predicted states $\{\mathbf{x}_{\ell|k}\}_{\ell=1}^\top$ and predicted inputs $\{\mathbf{u}_{\ell|k}\}_{\ell=0}^{T-1}$ can be defined as

$$x_{\ell|k}(\boldsymbol{\vartheta}_k, \mathbf{w}_k) = \Phi^0_{\ell|k}(\boldsymbol{\vartheta}_k)x_k + \Phi^v_{\ell|k}(\boldsymbol{\vartheta}_k)\mathbf{v}_k + \Phi^w_{\ell|k}(\boldsymbol{\vartheta}_k)\mathbf{w}_k \tag{8}$$

$$u_{\ell|k}(\boldsymbol{\vartheta}_k, \mathbf{w}_k) = K\Phi^0_{\ell|k}(\boldsymbol{\vartheta}_k)x_k + (K\Phi^v_{\ell|k}(\boldsymbol{\vartheta}_k) + \Gamma_\ell)\mathbf{v}_k + K\Phi^w_{\ell|k}(\boldsymbol{\vartheta}_k)\mathbf{w}_k, \tag{9}$$

Then, the matrix Φ_T is defined as

$$\Phi_T(\boldsymbol{\vartheta}_k) \doteq \begin{bmatrix} \Phi^0_{0|k}(\boldsymbol{\vartheta}_k) & \Phi^v_{0|k}(\boldsymbol{\vartheta}_k) & \Phi^w_{0|k}(\boldsymbol{\vartheta}_k) \\ \vdots & \vdots & \vdots \\ \Phi^0_{T|k}(\boldsymbol{\vartheta}_k) & \Phi^v_{T|k}(\boldsymbol{\vartheta}_k) & \Phi^w_{T|k}(\boldsymbol{\vartheta}_k) \end{bmatrix},$$

and the following are derived $\bar{Q} = \mathbb{I}_T \otimes Q$, $\bar{R} = \mathbb{I}_T \otimes R$, $\bar{K} = \mathbb{I}_T \otimes K$, and $\Gamma = [0_{mT\times n} \;\; \mathbb{I}_{mT} \;\; 0_{mT\times m_w T}]$, yielding

$$Q_E = M^\top \Phi_T^\top(\boldsymbol{\vartheta}_k)\begin{bmatrix} \bar{Q} & 0_{nT\times n} \\ 0_{n\times nT} & P \end{bmatrix}\Phi_T(\boldsymbol{\vartheta}_k)M$$

$$R_E = M^\top[\bar{K}\Phi_T(\boldsymbol{\vartheta}_k) + \Gamma]^\top \bar{R}[\bar{K}\Phi_T(\boldsymbol{\vartheta}_k) + \Gamma]M$$

where the matrix M is

$$M = \begin{bmatrix} \mathbb{I}_n & 0_{n\times mT} & 0_{n\times nT} \\ 0_{mT\times n} & \mathbb{I}_{mT} & 0_{mT\times nT} \\ 0_{nT\times n} & 0_{nT\times mT} & \mathbf{w}_k\mathbb{I}_{nT}. \end{bmatrix}$$

Given (8)–(9), the expected value of the finite-horizon cost (7) can be evaluated offline taking random samples of the sequences $\boldsymbol{\vartheta}_k$ and $\mathbf{w}_k$ (Mammarella et al., 2018b). This sample approximation leads to a quadratic cost of the form

$$J_T(x_k, \mathbf{v}_k) \approx \begin{bmatrix} x_k^\top & \mathbf{v}_k^\top & \mathbf{1}_n^\top \end{bmatrix} S \begin{bmatrix} x_k \\ \mathbf{v}_k \\ \mathbf{1}_n \end{bmatrix}, \tag{11}$$

with the explicit cost matrix S given by

$$S = \mathbb{E}\{(Q_E + R_E)\}. \tag{12}$$

As discussed in Lorenzen et al. (2017a), matrix S may be approximated via random sampling by exploiting classical Monte Carlo or Quasi Monte Carlo tools, as those presented in, e.g., Niederreiter (1992).

Remark 2. We observe that both the predicted state (8) and the predicted input (9) can be expressed as functions of the initial condition x_k at time k and the decision variable $\mathbf{v}_k$. Consequently, the deterministic cost function (11) also depends solely on x_k and $\mathbf{v}_k$.

To effectively solve the defined chance-constrained optimization (CCO) problem, it shall be properly recast as a tractable problem, thus extending its applicability. First, an approximation $\bar{\mathbb{X}}$ of the CCS $\mathbb{X}$ is computed. As described in Mammarella et al. (2022), three mainstream approaches can be identified to effectively deal with chance constraints: i) *exact techniques*, where the convexity of the constraints allows to efficiently compute the solution of the chance-constrained optimization problem as in, e.g., Prékopa (1995); ii) *robust approximations*, e.g., (Hewing & Zeilinger, 2018), where the goal is finding deterministic conditions that allow to build a guaranteed inner approximation of the probabilistic set; and iii) *sample-based approximations*, which are techniques based of random sampling of the uncertain parameters according to a given probability distribution, associating to each sample the corresponding *sampled* set and then enforcing some probabilistic guarantees (Lorenzen et al., 2017b).

In this paper, the focus is on the third class, where two complementary approaches, i.e., sequential and non-sequential, have been proposed. In the framework of non-sequential schemes, the original robustness problem is reformulated as a single optimization problem with sampled constraints, which are randomly generated according to a given probability distribution. A relevant feature of these methods is that they do not require any validation step and the sample complexity is fixed a priori. The goal is to derive an explicit lower bound on the required sample size to provide specific probabilistic guarantees. A classical approach for non-sequential methods is based upon statistical learning theory (Vidyasagar, 2013). In this paper, the results based on the latter line of research (see, e.g., Alamo et al. (2009, 2015)) are exploited to approximate the chance-constrained set $\mathbb{X}$ and make the CCO computationally tractable.

In the specific case, the goal is to defined a tractable approximation of the CC set $\mathbb{X}_\varepsilon$ defined as

$$\mathbb{X}_\varepsilon = \bigcup_{\substack{\ell=0,\ldots,N-1 \\ j=1,\ldots,p}} \mathbb{X}_\ell^{P,j} \tag{13}$$

composed by single chance constraints of the form

$$\mathbb{X}_{\ell}^{P,j} = \left\{ x_k, \mathbf{v}_k \mid \mathsf{Pr}\left\{ [H_x]_j x_{\ell|k}(\boldsymbol{\vartheta}_k, \mathbf{w}_k) \leq [h_x]_j \right\} \geq 1 - \varepsilon \right\},$$

relying on the results of statistical learning theory applied on the so-called (α, k)-Boolean functions given in Alamo et al. (2009). Specifically, it was demonstrated that if one extract a sufficient number N_{ℓ}^{x} of iid sample sequences $\boldsymbol{\vartheta}^{(i)}$ and $\mathbf{w}^{(i)}$ to build the sample constraint set

$$\mathbb{X}_{\ell}^{S,j} = \left\{ x_k, \mathbf{v}_k \mid [H_x]_j x_{\ell|k}(\boldsymbol{\vartheta}^{(i_\ell)}, \mathbf{w}^{(i_\ell)}) \leq [h_x]_j, i_\ell \in \mathbb{N}_1^{N_\ell^x} \right\}, \tag{14}$$

for $\ell \in \mathbb{N}_0^{T-1}$, with probability not smaller than $1 - \delta$ it is guaranteed that $\mathsf{Pr}\left\{ \mathbb{X}_{\ell}^{S} \subseteq \mathbb{X}_{\ell}^{P} \right\}$. Among the results presented in Alamo et al. (2009), those inherited from Alamo et al. (2009, Theorem 8) are recalled in the following proposition.

Proposition 1. *For any violation level $\varepsilon \in (0, 0.14)$ and confidence level δ, if the number N_s of iid samples is chosen so that $N_{\ell}^{x} \geq N_{LT}$, with N_{LT} the sample size bound defined as*

$$N_{LT} = \frac{4.1}{\varepsilon}\left(\ln \frac{21.64}{\delta} + 4.39n \log_2\left(\frac{8e}{\varepsilon}\right)\right),$$

then $\mathsf{Pr}\left\{ \mathbb{X}_{\ell}^{S} \subseteq \mathbb{X}_{\ell}^{P} \right\} \geq 1 - \delta$.

This proposition implies that, with confidence $1 - \delta$, all feasible points of the sampled constraints (14) satisfy the chance constraint in (4). Analogous sample size bounds can be computed for the input constraints, once the set $\mathbb{U}$ is approximated by sampled constraints, and for the terminal region $\mathbb{X}_T$.

The sampling procedure employed to compute the approximation of the CC set $\mathbb{X}_{\epsilon}$ leads to a set of $N_x = \sum_{\ell=0}^{T-1} N_{\ell}^{x}$ linear constraints that can be rewritten in a compact form combining (8) with (14). In this way, one obtains

$$\begin{bmatrix} \tilde{H}_x^x & \tilde{H}_x^u \end{bmatrix} \begin{bmatrix} x_k \\ \mathbf{v}_k \end{bmatrix} \leq \tilde{h}_x, \quad i_\ell \in \mathbb{N}_1^{N_\ell^x}$$

where the matrices $\begin{bmatrix} \tilde{H}_x^x & \tilde{H}_x^u \end{bmatrix}$ and vector $\tilde{h}_x$ are defined as

$$[\tilde{H}_x^x \;\; \tilde{H}_x^u] = \left[H_x \Phi_{\ell|k}^{0}(\boldsymbol{\vartheta}^{(i_\ell)}) \quad H_x \Phi_{\ell|k}^{v}(\boldsymbol{\vartheta}^{(i_\ell)}) \right],$$

$$\tilde{h}_x = \left[h_x - H_x \Phi_{\ell|k}^{w}(\boldsymbol{\vartheta}^{(i_\ell)}) \mathbf{w}_k^{(i_\ell)} \right],$$

with $\ell \in \mathbb{N}_0^{T-1}$ and $i_\ell \in \mathbb{N}_1^{N_\ell^x}$. Then, in a similar way, it is possible to sample-approximate the input and terminal constraint sets, such that they are reformulated in a compact form as follows

$$\begin{bmatrix} \tilde{H}_u^x & \tilde{H}_u^u \end{bmatrix} \begin{bmatrix} x_k \\ \mathbf{v}_k \end{bmatrix} \leq \tilde{h}_u, \quad \begin{bmatrix} \tilde{H}_T^x & \tilde{H}_T^u \end{bmatrix} \begin{bmatrix} x_k \\ \mathbf{v}_k \end{bmatrix} \leq \tilde{h}_T.$$

Finally, it is possible to stack all constraint into a single set as follows

$$\begin{aligned} \mathbb{D} &= \left\{ x_k, \mathbf{v}_k \;\middle|\; \begin{bmatrix} \tilde{H}_x^x & \tilde{H}_x^u \\ \tilde{H}_T^x & \tilde{H}_T^u \\ \tilde{H}_u^x & \tilde{H}_u^u \end{bmatrix} \begin{bmatrix} x_k \\ \mathbf{v}_k \end{bmatrix} \leq \begin{bmatrix} \tilde{h}_x \\ \tilde{h}_T \\ \tilde{h}_u \end{bmatrix} \right\} \\ &= \left\{ x_k, \mathbf{v}_k \;\middle|\; \tilde{H} \begin{bmatrix} x_k \\ \mathbf{v}_k \end{bmatrix} \leq \tilde{h} \right\}. \end{aligned} \tag{15}$$

Due to the sampling procedure, these linear constraints are in general highly redundant. To cope with this issue, it is possible to rely on suitable algorithms for redundant constraints removal so that these sets can be further simplified. A simple algorithm to remove redundant constraints is presented in Lorenzen et al. (2017b) and described in Algorithm 1.

More sophisticated tools can be found, e.g., in the Matlab MPT toolbox. Another possibility is presented in Mammarella et al. (2022) where a probabilistic scaling approach is proposed that, when applied to a low-complexity simple approximating set (e.g., an ℓ_p-ball), it allows to significantly reduce the sample complexity and the computational load.

Algorithm 1 Redundant constraint removal procedure.

Require: Constraint $Hx \leq h$, $H \in \mathbb{R}^{n_c \times n}$, $h \in \mathbb{R}^{n_c}$

$i \leftarrow 1$
while $i \leq n_c$ **do**
  Solve

$$h_i^\star = \max_x [H]_i x, \text{ s.t. } [H]_k x \leq [h]_k, \ \forall k \in \mathbb{N}_1^{n_c} \setminus i$$

  if $h_i^\star \leq [h]_i$ **then**
    $H \leftarrow H \setminus [H]_i, \quad h \leftarrow h \setminus [h]_i, \quad n_c \leftarrow n_c - 1$
  else
    $i \leftarrow i + 1$
  end if
end while
return H, h

Last, having considered bounded uncertainties that are sampled offline, the constraints can be suitably augmented in such a way that recursive feasibility is recovered. This is done by adding a first-step constraint set $\mathbb{D}_R$ to (15) as follows.

Let

$$\mathbb{C}_T = \left\{ \begin{bmatrix} x_k \\ v_{0|k} \end{bmatrix} \mid \exists\, v_{1|k}, \dots, v_{T-1|k}, \text{ s.t. } (x_k, v_k) \in \mathbb{D} \right\},$$

be the T-step set and feasible first input, i.e., the set of feasible states and first inputs of the finite horizon scenario program for given fixed samples $\boldsymbol{\vartheta}_k^{(i)}$. Let

$$\mathbb{C}_{T,x}^{\infty} = \{ x_k \mid H_\infty x_k \leq h_\infty \},$$

be a (maximal) robust control invariant polytope for the system (3) with $(x_k, u_k) \in \mathbb{C}_T$. This second set can be computed via standard recursion (see e.g., Kerrigan (2000)). Then, in order for the OS-SMPC optimization to be robustly recursively feasible, the constraint set is added

$$\mathbb{D}_R = \left\{ x_k, \mathbf{v}_k \mid H_\infty A_K^{\iota} x_k + H_\infty B^{\iota} v_{0|k} \leq h_\infty, \ \iota \in \mathbb{N}_1^{N_c} \right\} \tag{16}$$

with $A_K^{\iota} = A^{\iota} + B^{\iota} K$ and A^{ι}, B^{ι} from Assumption 2.

Finally, Algorithm 2 summarizes the proposed OS-SMPC approach, exploited in the sequel for the attitude control of the LEO nano-satellite.

Algorithm 2 OS-SMPC algorithm.

Offline step.
Compute the expected value of S (12).
Design the set $\mathbb{D}$ (15).
Determine the first–step constraint set $\mathbb{D}_R$ (16).
Online implementation. At each time k:
Measure the current state x_k.
Solve the approximated CCO problem

$$\begin{aligned} \mathbf{v}_k^\star \;:=\; & \arg\min_{\mathbf{v}_k} \; J_T(x_k, \mathbf{v}_k) \\ & \text{s.t. } (x_k, \mathbf{v}_k) \in \mathbb{D} \cap \mathbb{D}_R. \end{aligned} \tag{17}$$

return $u_k = v_{0|k}^\star + K x_k$ with $v_{0|k}^\star$ the first control action of $\mathbf{v}_k^\star$.

4. Properties of OS-SMPC scheme

In this section, the properties in terms of recursive feasibility and closed-loop chance-constraint satisfaction of the OS-SMPC scheme are recalled, as already proved in Mammarella et al. (2018b). Then, a stochastic descent property of the cost function is demonstrated. This property implies that eventually the closed-loop trajectories will converge to a neighborhood of the origin.

4.1. Recursive feasibility and constraint satisfaction

The introduction of the first step constraint $\mathbb{D}_R$ allows to prove recursive feasibility of the OS-SMPC scheme. In detail, let

$$\mathbb{V}(x_k) = \left\{ \mathbf{v}_k \in \mathbb{R}^{mT} \mid (x_k, \mathbf{v}_k) \in \mathbb{D} \cap \mathbb{D}_R \right\}.$$

If $\mathbf{v}_k \in \mathbb{V}(x_k)$, then the OS-SMPC guarantees

$$\mathbb{V}(x_{k+1}) \neq \emptyset.$$

Moreover, since the OS-SMPC algorithm is robustly recursively feasible, then hard input constraint satisfaction is guaranteed because of $H_u u_{0|k} \leq h_u$, which does not rely on sampling. On the other hand, for each sampled constraint, it holds that $\mathbb{D} \subseteq \mathbb{X}_{\ell=1}^{S,j}$, for $j = \mathbb{N}_1^p$. Hence, if $x_0 \in \mathbb{C}_{T,x}^{\infty}$, then the closed-loop system under the OS-SMPC control law, for all $k \geq 1$, satisfies each probabilistic state constraint (4) with confidence $1 - \delta$.

4.2. Probabilistic conditions on $V_T(x_k)$

In this section, a stochastic descent property of the expected value of the optimal solution (17) is derived by applying the law of total expectation. The following assumption is instrumental to demonstrate that the cost increase is bounded if the candidate solution does not remain feasible for a given probability ε_f.

Assumption 4. Let $V_T(x_k)$ be the optimal value function of Problem (17), and let $P_\ell,\ P_u \in \mathbb{R}^{n\times n},\ P_\ell \succ 0,\ P_u \succ 0,\ c \in \mathbb{R}$ be such that $x_k^\top P_\ell x_k \leq V_T(x_k) - c \leq x_k^\top P_u x_k$ holds for all $x_k \in \mathbb{C}_{T,x}^{\infty}$, where c is a constant term related to the presence of additive disturbance.

Theorem 1 (Stochastic descent property). *Let $V_T(x_k) = J_T(x_k, \mathbf{v}_k^\star)$ be the optimal value of (17) at time k. Let the i.i.d. random noise $w_k \in \mathbb{R}^n$ be such that $\mathbb{E}\{w_k\} = 0$ and $\mathbb{E}\{w_k w_k^\top\} = \Gamma_w$ for all $k \in \mathbb{N}$. If Assumption 2 and Assumption 4 hold, then for $x_0 \in \mathbb{C}_{T,x}^{\infty}$*

$$\mathbb{E}_{w_k}\{V_T(x_{k+1})\} - V_T(x_k) \leq -(1-\varepsilon_f)\lambda_{min}\|x_k\|_2^2 + C(\varepsilon_f),$$

with $\varepsilon_f \in [0,1)$ the probability that the candidate solution is not feasible and $\lambda_{\min}$ as a lower bound on the smallest eigenvalue of

$$U(\vartheta_k) = \begin{bmatrix} M_{11} & M_{12} \\ M_{21} & M_{22} \end{bmatrix} \tag{18}$$

with

$$M_{11} = Q - \frac{2\varepsilon_f}{1-\varepsilon_f}\left(A_K(\vartheta_k)^\top P_u A_K(\vartheta_k) - \frac{1}{2}P_\ell\right)$$

$$M_{12} = M_{21}^\top = -\frac{2\varepsilon_f}{1-\varepsilon_f} A_K(\vartheta_k)^\top P_u B(\vartheta_k)$$

$$M_{22} = -\frac{2\varepsilon_f}{1-\varepsilon_f} B(\vartheta_k)^\top P_u B(\vartheta_k),$$

and $C(\varepsilon_f)$ a bounded quantity defined as

$$C(\varepsilon_f) = (1-\varepsilon_f)\mathrm{tr}\left(P\Gamma_w\right) + 2\varepsilon_f \max_{w_k \in \mathbb{W}} \|w_k\|_{P_u}^2. \tag{19}$$

Proof. Let $V_T(x_k) = J_T(x_k, \mathbf{v}_k^*)$ be the optimal value of (17) at time k and consider the optimal value function of the online optimization program as stochastic Lyapunov function. Hence, if the candidate solution $\tilde{\mathbf{v}}_{k+1}$ remains feasible, then

$$\begin{aligned}
&\mathbb{E}_{w_k}\left\{V_T(x_{k+1}),\ \tilde{\mathbf{v}}_{k+1} \text{ feasible}\right\} - V_T(x_k) \\
&\leq \mathbb{E}_{w_k}\left\{J_T(x_{k+1}, \tilde{\mathbf{v}}_{k+1})\right\} - V_T(x_k) \\
&\leq \mathbb{E}_{w_k}\left\{\sum_{l=0}^{T-1}(\|x_{\ell|k+1}\|_Q^2 + \|u_{\ell|k+1}\|_R^2) + \|x_{T|k+1}\|_P^2\right\} \\
&\quad - \left(\sum_{l=0}^{T-1}(\|x_{\ell|k}^\star\|_Q^2 + \|u_{\ell|k}^\star\|_R^2) + \|x_{T|k}^\star\|_P^2\right) \\
&= \mathbb{E}_{w_k}\left\{\|x_{T|k}^\star\|_{Q+K^\top RK-P}^2 + \|A_K(\vartheta_k)x_{T|k}^\star + w_{k+T}\|_P^2\right\} \\
&\quad - \|x_k\|_Q^2 - \|u_{0|k}^\star\|_R^2 \\
&\leq \mathbb{E}_{w_k}\left\{\|w_{k+T}\|_P^2\right\} - \|x_{0|k}^*\|_Q^2 - \|u_{0|k}^*\|_R^2 \\
&\leq \mathrm{tr}\left(P\Gamma_w\right) - \|x_k\|_Q^2.
\end{aligned}$$

On the other hand, if the candidate solution does not remain feasible, the cost increase can be bounded through the matrices in Assumption 4. Hence, if the candidate solution is found to be infeasible,

$$\begin{aligned}
&\mathbb{E}_{w_k}\left\{V_T(x_{k+1}),\ \tilde{\mathbf{v}}_{T|k+1} \text{ not feasible}\right\} - V_T(x_k) \\
&\leq \max_{\substack{w\in\mathbb{W} \\ (A(\vartheta_k),B(\vartheta_k))\in\mathbb{G}}} \|A(\vartheta_k)x_k + B(\vartheta_k)u_k + w_k\|_{P_u}^2 - \|x_k\|_{P_\ell}^2 \\
&\leq \max_{\substack{w\in\mathbb{W} \\ (A(\vartheta_k),B(\vartheta_k))\in\mathbb{G}}} \Big(\|A_K(\vartheta_k)x_k + B(\vartheta_k)v_k\|_{P_u}^2 + \|w_k\|_{P_u}^2 \\
&\quad + 2\left\|\left(A_K(\vartheta_k)x_k + B(\vartheta_k)v_k\right)^\top P_u w_k\right\|\Big) - \|x_k\|_{P_\ell}^2 \\
&\leq 2\max_{(A(\vartheta_k),B(\vartheta_k))\in\mathbb{G}}\left(\|A_K(\vartheta_k)x_k + B(\vartheta_k)v_k\|_{P_u}^2\right) \\
&\quad + 2\max_{w_k\in\mathbb{W}}\|w_k\|_{P_u}^2 - \|x_k\|_{P_\ell}^2.
\end{aligned}$$

Given a lower bound $\lambda_{\min}$ on the smallest eigenvalue of (18), it holds that

$$\begin{aligned}
-\begin{bmatrix} x_k & v_k \end{bmatrix} U(\vartheta_k) \begin{bmatrix} x_k \\ v_k \end{bmatrix} &\leq -\lambda_{min}\left(\|x_k\|_2^2 + \|v_k\|_2^2\right) \\
&\leq -\lambda_{min}\|x_k\|_2^2.
\end{aligned}$$

Then, defined the parameter $C(\varepsilon_f)$ as in (19) and applying the law of total expectation, it follows that

$$\begin{aligned}
&\mathbb{E}_{w_k}\left\{V_T(x_{k+1}),\ \tilde{\mathbf{v}}_{T|k+1}\right\} - V(x_k) \\
&\leq \varepsilon_f\Big(2\max_{(A(\vartheta_k),B(\vartheta_k))\in\mathbb{G}}\|A_K(\vartheta_k)x_k + B(\vartheta_k)v_k\|_{P_u}^2 \\
&\quad + 2\max_{w\in\mathbb{W}}\|w_k\|_{P_u}^2 - \|x_k\|_{P_\ell}^2\Big) \\
&\quad + (1-\varepsilon_f)\Big(\mathrm{tr}\left(P\Gamma_w\right) - \|x_k\|_Q^2\Big) \\
&= \varepsilon_f\Big(2\max_{(A(\vartheta_k),B(\vartheta_k))\in\mathbb{G}}\|A_K(\vartheta_k)x_k + B(\vartheta_k)v_k\|_{P_u}^2\Big) \\
&\quad - (1-\varepsilon_f)\|x_k\|_Q^2 - \varepsilon_f\|x_k\|_{P_\ell}^2 \\
&\quad + (1-\varepsilon_f)\mathrm{tr}\left(P\Gamma_w\right) + 2\varepsilon_f\max_{w_k\in\mathbb{W}}\|w_k\|_{P_u}^2 \\
&\leq -(1-\varepsilon_f)\lambda_{min}\|x_k\|_2^2 + C(\varepsilon_f),
\end{aligned}$$

which concludes the proof. □

Corollary 1. *Defined the region $\mathcal{K}$ as*

$$\mathcal{K} = \left\{ x_k \in \mathbb{R}^n \mid x_k^\top x_k \leq \frac{C(\varepsilon_f)}{(1-\varepsilon_f)\lambda_{min}} \right\},$$

it follows that

$$\mathbb{E}_{w_k}\left\{V_T(x_{k+1})\right\} - V(x_k) < 0, \quad \text{for all } x_k \notin \mathcal{K}.$$

Furthermore, if $\mathcal{K} \subseteq \mathbb{X}_T$, the optimal cost $V(x_k)$ decrease in expectation as long as $x_k \notin \mathbb{X}_T$.

Proof. The proof is straightforward and the corollary aims to obtain a less conservative condition on the stochastic descent properties of the cost function with respect to the one given by Theorem 1. □

Theorem 1 together with Corollary 1 state that the system contracts toward a compact set $\mathcal{K}$. Let us assume that the terminal set $\mathbb{X}_T$ has the form

$$\mathbb{X}_T = \{x \in \mathbb{R}^n : x^\top P x \leq \alpha\},$$

for some $\alpha > 0$ chosen such that $x \in \mathbb{X}$, $Kx \in \mathbb{U}$, and robust forward invariance is guaranteed. Equivalently, in the Euclidean norm, this implies $\|x\|_2^2 \leq \alpha/\lambda_{\max}(P)$. Then, the inclusion $\mathcal{K} \subseteq \mathbb{X}_T$ is satisfied if and only if

$$\alpha \geq \frac{\lambda_{\max}(P)}{(1-\varepsilon_f)\lambda_{\min}} C(\varepsilon_f).$$

This condition emphasizes that the assumption $\mathcal{K} \subseteq \mathbb{X}_T$ can be satisfied only under sufficiently small disturbance and uncertainty levels, or for a sufficiently small ε_f, ensuring that the ultimate boundedness set resulting from the stochastic Lyapunov analysis is contained within the terminal invariant set.

Hence, if $\mathcal{K} \subseteq \mathbb{X}_T$ and $x_0 \in \mathbb{C}^{\infty}_{T,x}$, the geometric drift condition guarantees that the closed-loop trajectories enter the terminal region $\mathbb{X}_T$ in finite time. Moreover, since $\mathbb{X}_T$ is robustly forward invariant for (3) under the control law $u_k = Kx_k$, the closed-loop trajectory remains in $\mathbb{X}_T$ with probability 1 thereafter. This property can then be used to show that $\mathbb{X}_T$ is asymptotically stable in probability for the system (3) (Lorenzen et al., 2017a, Definition 4).

5. High-fidelity simulation results

5.1. Mission scenario and pointing requirements

For the validation of the proposed OS-SMPC scheme, an EO scenario involving small satellites operated in low orbits is selected. Specifically, a 3U platform is considered, with standardized geometry ($0.1 \times 0.1 \times 0.3405$ cm) and mass (3.95 kg), operated on an elliptical LEO orbit (eccentricity: 0.002) with a 6924.1 km semi-major axis, 187.48° inclination, with a 193.5507° RAAN and a 224.7226° argument of periapsis. The nadir-pointing mission profile is then defined following the guidelines provided in Ott et al. (2011), consistent with and elaborating the ECSS standard ECSS-E-ST-60-10C (2008) for the specific case of satellite pointing error.

In detail, the following ingredients are defined as instrumental to the definition of the performance requirements, having considered time-random pointing error sources, e.g., environmental disturbances and system dynamics induced errors: i) required error value with respect to the angular deviation per body axis $e_p = 10^{-2}$ rad (i.e., 0.537°); ii) required error value with respect to the angular rate magnitude per body axis $e_r = 10^{-2}$ rad/s (i.e., $0.537°/s$); iii) mixed statistical interpretation of the ensemble of pointing error realizations; iv) absolute pointing error (APE) as error index to be constrained, defined as the difference between the target parameter (attitude or angular rate) and the actual parameter in the chosen reference frame; v) evaluation period equal to 10% of the orbital period; and vi) level of confidence P_c so that the violation level shall be lower than ε with confidence level δ.[3] Accordingly, requirements on both attitude and angular rate deviation per body axis are defined as chance constraints of the form

$$\Pr\left\{ \|e_k^{(i)}\|_\infty \leq e_{ref} \right\} \geq P_c,$$

considering the ensemble of realization i and in time k. We note that points i) and ii) together with e_p and e_r determine the set $\mathbb{X}$ and the corresponding H_x and h_x.

Moreover, the enforced requirements are assumed to represent operational mode transition requirements, valid at any time during the mission when the satellite is commanded to go to nadir-pointing mission mode. Then, defining the reference operational envelope (or initial feasible set) for attitude and angular rate so that the initial conditions for each body axis are sampled as follows,

$$\|(\phi, \theta, \psi)\|_\infty \leq 20°, \quad \|(\omega_x, \omega_y, \omega_z)\|_\infty \leq 2°/\text{s},$$

the performance requirements can now be stated, having been embedded in the design of the control scheme as state chance constraints.

REQ-AOCS-MODE-010:*Starting from any initial attitude and angular rate condition within the specified operational envelope, the satellite shall reorient and stabilize to the nadir-pointing mission attitude with an absolute pointing error of* $\leq 0.5°$ *about each body axis, with a confidence level of* $(1-\varepsilon)\times 100\%$*, evaluated over a time interval equal to* 10% *of the orbital period, starting from the time the transition to nadir-pointing mission mode is commanded.*

REQ-AOCS-MODE-020: *Starting from any initial attitude and angular rate condition within the specified operational envelope, the satellite shall reorient and stabilize to the nadir-pointing mission mode with a residual angular rate magnitude of* $\leq 0.5°/s$ *about each body axis, with a confidence level of* $(1-\varepsilon)\times 100\%$*, evaluated over a time interval equal to* 10% *of the orbital period, starting from the time the transition to nadir-pointing mission mode is commanded.*

Last, the following requirement on the attitude actuator are set, so that the associated the hard input constraint set is defined as follows

$$u_k \in \mathbb{U} = \left\{ u \in \mathbb{R}^3 \mid \|u\|_\infty \leq 10^{-3} \right\}.$$

REQ-AOCS-ACT-010: *The spacecraft shall limit the commanded control torque vector to a maximum magnitude of* 1×10^{-3} *Nm about each body axis during all operational modes.*

5.2. Simulation and controller settings

All simulations were carried out using the EOSS simulator discussed in Section 2. The EOSS simulator run over a Intel® Core™ i9 – 10980HK CPU @3.10GHz with a 32GB RAM. For the model implementation settings, the attitude dynamics update time is set to 0.01s and selected onboard sensors update rates between 5Hz and 20Hz. In contrast, the control update time was determined through a trade-off analysis considering real-time implementability, as discussed in Section 5.3. To solve the optimization problem underlying each MPC scheme the quadratic programming solver *quadwright* Currie et al. (2012), able to speed up the computational capabilities for embedded applications, is employed. The following quadwright settings have been used: i) 100 as maximum number of iterations; and ii) 10^{-8} for the tolerance level.

To better highlight the improvements achievable with a stochastic scheme, the performance of the OS-SMPC approach described in this paper is compared against: i) a (more optimistic) classical MPC scheme neglecting uncertainty and simply minimizing a linear quadratic cost (LQMPC), and ii) a (more conservative) robust MPC solution implementing a classical tube-based approach (TRMPC) as presented in Mammarella et al. (2018a).

All three MPC cost weight matrices were set to $Q = 10^6\mathbb{I}_6$ and $R = 10^3\mathbb{I}_3$, where the specific numerical values were selected based on the relative scaling of states and inputs and the tightness of the associated chance constraints, and were validated through closed-loop simulations. For the TRMPC and the OS-SMPC, the same robustly stabilizing feedback gain matrix K was designed offline using classical robust tools for the solution of LMIs (e.g., Lofberg (2004)) using a standard SDP solver (e.g., SeDuMi/SDPT3). Moreover, for all three controllers, the prediction horizon is set to $N = 5$.

Next, the effects of the control update interval dt and the number of samples N_s (the latter relevant only for the stochastic scheme) on the computational effort required to assess the real-time implementability of the controllers are first evaluated. Then, the performance of the three MPC schemes in terms of pointing-tracking capabilities and control effort are compared. Finally, the combined impact of the payload FOV and the control scheme performance on coverage accuracy are examined.

5.3. Effects of control update rate

In this section, the real-time implementability of each control scheme is assessed for the different update rates. We assume that the platform is equipped with an OBC-Cube-Polar CubeSat onboard computer, featuring a quad-core 64-bit RISC-V processor running at approximately 660 MHz for a combined performance exceeding 4,000 DMIPS, supported by 2–4 GB of ECC RAM. The real-time feasibility is evaluated by estimating the OBC execution time from the runtime measured on the laptop, scaled according to the ratio of their computational performance. Specifically, assuming that the laptop used for the simulations

[3] The probabilistic levels P_c, ε and δ are selected with respect to the sample complexity and associated computational load, as analyzed in Section 5.4.

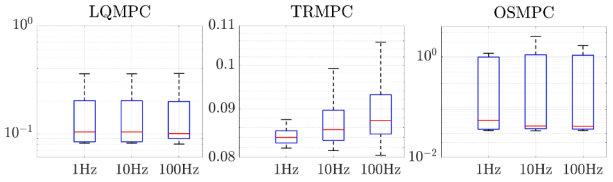

Fig. 2. Expected computational cost for running the three MPC schemes over the OBC-Cube-Polar board.

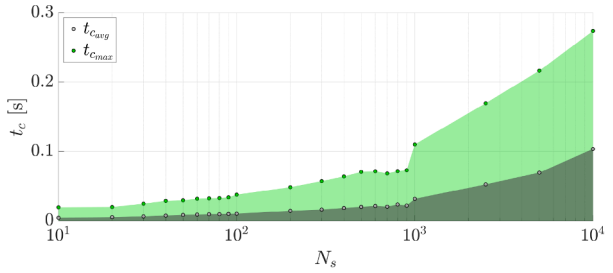

Fig. 3. Average and maximum t_c for varying N_s.

delivers approximately 100,000 DMIPS and the OBC-Cube-Polar provides about 4,000 DMIPS, the expected onboard computation time $t_{c,\text{sat}}$ can be approximated as

$$t_{c,\text{sat}} \approx \frac{DMIPS_{\text{laptop}}}{DMIPS_{\text{sat}}} t_c.$$

Accordingly, Fig. 2 reports the expected computational load corresponding to the execution of the algorithms on the target hardware.

In detail, Fig. 2 shows the effect of the control update rate on the computational load for the three schemes. The box-plot illustrates the distribution of the computational time t_c for rates equal to 1, 10, and 100 Hz. Each box shows the inter-quartile range (IQR), with the median as a (red) horizontal line and whiskers extending to 1.5×IQR for 100 simulations running over one orbit, each one starting from a different initial condition.

First, it can be observed that, regardless of the selected control update rate, all case studies exhibit similar t_c values for the 25% and 75% percentile. On the other hand, it can be observed that, when considering the median value, all three algorithms would satisfy the real-time implementability requirement only for $dt = 0.1$ s.

5.4. Effects of sample size

With the control update rate set to 10Hz, the impact of the sample complexity N_s on the computational time t_c of the OS-SMPC is assessed. Fig. 3 shows the maximum and average values of t_c computed over a single orbit, using the same initial condition. We observe that for $N_s \approx 10,000$, the average computation time $\bar{t}_c$ satisfies $\bar{t}_c \leq dt$, thus ensuring real-time implementability. Smaller N_s further reduce the computational effort, but at the expense of increased violation levels. Specifically, for $N_s \leq 1,000$, real-time feasibility of the OS-SMPC online implementation is always preserved, in spite of much larger violation levels.

In line with this analysis, the sample complexity is set to $N_s = 10,000$ for the following set of simulations, which correspond to probabilistic levels $\varepsilon = 0.14$ and $\delta = 10^{-6}$.

Remark 3. It is worth noting that comparable coverage performance is achieved regardless of the selected control update time dt, with only minor variations observed when adjusting the sample size N_s.

5.5. Comparing performance against predictive scheme

Having selected $dt = 0.1$s and $N_s = 10,000$ according to the analyzes discussed in Section 5.3 and Section 5.4, the three predictive control strategies are now compared in terms of pointing accuracy and control effort. To ensure the robustness of these analyses, a total of 100 simulations are run, each with a duration of one orbital period and starting from a different set of Euler angles and angular rate. Specifically, the initial conditions for attitude and angular rate are sampled from normal distributions, truncated to maximum amplitude of 10° and 0.1 rad/s, respectively.

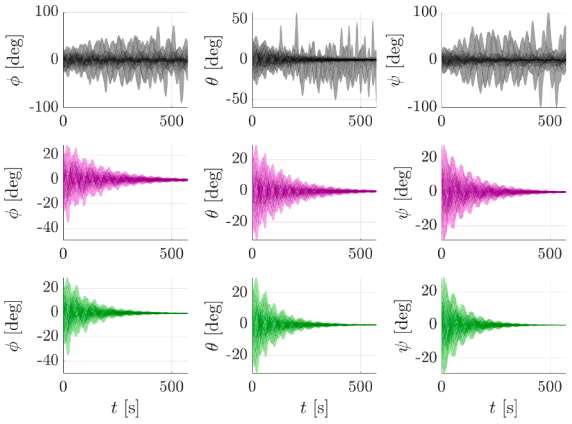

Fig. 4. Controlled evolution of the satellite attitude obtained with classic (black), robust (magenta), and stochastic (green) MPC for 100 initial conditions. (For interpretation of the references to colour in this figure legend, the reader is referred to the web version of this article.)

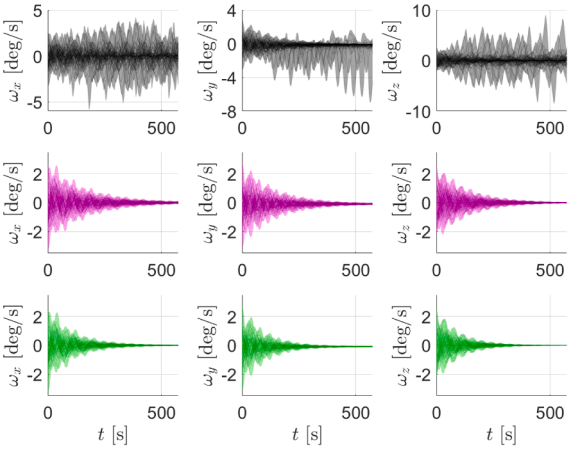

Fig. 5. Controlled evolution of the satellite angular rate obtained with classic (black), robust (magenta), and stochastic (green) MPC for 100 initial conditions. (For interpretation of the references to colour in this figure legend, the reader is referred to the web version of this article.)

Fig. 4 shows the controlled attitude dynamics, expressed in terms of Euler angles, under the effect of both environmental disturbances and sensor noise. Across 100 simulations, most runs employing the LQMPC scheme are heavily affected by these disturbances, resulting in a loss of the expected pointing accuracy. On the other hand, both TRMPC and OS-SMPC are able to steer the trajectories toward zero, regardless of the initial orientation of the satellite. Moreover, one can also notice that the stochastic approach not only achieves a shorter settling time than the robust one but also drives the attitude closer to the desired nadir-pointing direction, thus guaranteeing improved pointing performance and coverage accuracy.

The performance of the three controllers are confirmed also for the angular rate dynamics, as shown in Fig. 5. The ability to steer and maintain the angular rate close to zero despite the effect of disturbances is of particular relevance for the image quality in EO scenarios. Indeed, if the angular velocity is not sufficiently low this may cause blur effects, thus compromising the efficacy of acquisition.

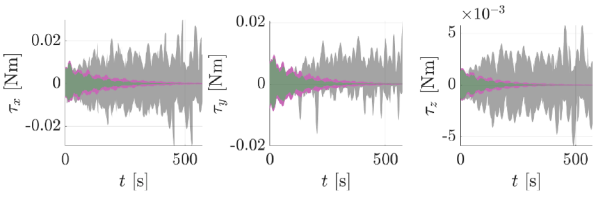

Fig. 6. Comparison of the control torque required by classic (black), robust (magenta), and stochastic (green) MPC for 100 initial conditions. (For interpretation of the references to colour in this figure legend, the reader is referred to the web version of this article.)

The last performance metric used to compare the three control schemes is the control effort, represented in Fig. 6 as the control torque required over one orbit for each approach. This quantity can be directly related to the energy consumption needed to operate the actuators (e.g., reaction wheels). It is first observed that the LQMPC exhibits the largest torque excursions, due to the attempts of rejecting the effects of disturbance torques on the rotational dynamics. In contrast, both the robust and stochastic MPC schemes exhibit a convergent trend toward zero torque after an initial transient phase. This behavior is intrinsic to their ability to reject disturbances, which are explicitly accounted for in their design. Moreover, as already observed in the rendezvous framework (see Mammarella et al. (2018b)), the OS-SMPC requires a lower control demand along all three directions compared to the more conservative robust approach.

Overall, Fig. 4 and Fig. 6 show that the OS-SMPC approach not only achieves faster convergence to the desired tracking direction but also demonstrates higher energy efficiency compared to the other schemes.

Next, the translation of the control performance of these predictive schemes into the two core aspects of Earth-observation satellites is analyzed: the pointing error, θ_{err}, and the projected coverage area, the latter evaluated with respect to the payload's FOV.

5.6. Control impact on pointing error

Considering a pointing scene, the pointing error θ_{err} is described with respect to the target plane, which in a EO scenario is defined as the Earth surface (ground) plane onto which the sensor line-of-sight intersects (Ott et al., 2011). Specifically, in this paper θ_{err} is intended as the absolute performance error, i.e., the difference between the target (commanded) attitude of the satellite q_{id}, in this case nadir-pointing, and the actual satellite attitude q_R. This parameter, together with the angular rate, is directly linked to image quality and ground coverage accuracy. Given the attitude error quaternion $q_{err} = q_{id}^{-1} \otimes q_R$, the pointing error is computed as $\theta_{err} = 2\arccos(|q_{err,0}|)$, where $q_{err,0}$ denotes the scalar component of q_{err}. Hence, values larger than zero indicate a misalignment of that many degrees between the boresight (often the payload optical axis) and the intended direction. And the misalignment would reflect over the overlapping among the projected ellipsoids $\mathcal{E}_{id}$ and $\mathcal{E}_R$ of the ideal cone and real one, respectively.

Fig. 7 summarizes the performance of the three MPC schemes in terms of: i) the time evolution of the pointing error over one orbit, ii) the histogram of the error distribution, and iii) the cumulative probability function (CPF) of the pointing error. The time-history plots (left column) confirm that both TRMPC and OS-SMPC outperform the classical approach in terms of settling time and constraint satisfaction under disturbances. This is quantitatively supported by the histograms of the pointing error distribution (center column), which show that, for the selected case study, TRMPC achieves the lowest mean error (0.597°), while OS-SMPC exhibits the smallest standard deviation (1.673°). On the other hand, LQMPC is consistently outperformed by both approaches. Finally, the CPF plots (right column) further emphasize this performance gap. Indeed, the probability of maintaining the error below 1° over three orbits is remarkably low for LQMPC (0.9) but exceeds 95% for both robust and stochastic MPC schemes.

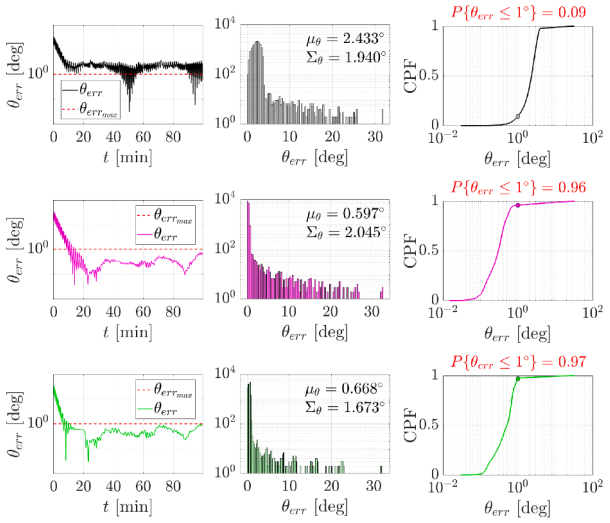

Fig. 7. Analysis of the pointing error statistics for LQMPC (black), TRMPC (magenta), and OS-SMPC (green) on data collected over three orbital periods. (For interpretation of the references to colour in this figure legend, the reader is referred to the web version of this article.)

5.7. Control impact on coverage

Let us consider a satellite equipped with a payload that has a given FOV, and for the coverage model let us assume a spherical shape of the Earth.

Remark 4. In this work, terrain elevation may be incorporated via an effective Earth radius offset h_t so that the footprint half-angle $\varkappa$ becomes

$$\varkappa = \arccos\left(\frac{R_\oplus + h_t}{R_\oplus + h}\cos(\varsigma)\right),$$

with $R_\oplus$ the Earth radius, h the satellite altitude, and ς the boresight angle (i.e., the half-cone angle of the satellite payload).

Then, the footprint of the antenna (i.e., the coverage area) is obtained as a part of the Earth's surface within the inner part of the right circular cone, whose origin is at the position of the satellite in its orbit, symmetry axis goes through the subsatellite point on the Earth, and the aperture corresponds to the antenna's FOV (or boresight angle ς). The Earth central angle θ_{cap}, whose value are used as a limiting condition to find all the points on the Earth surface that fall into the instantaneous coverage area of the payload, can be computed as

$$\theta_{cap} = 2\arcsin\left(\frac{R_\oplus + h}{R_\oplus}\right)\tan(\varsigma).$$

Remark 5. Non-ideal footprint behavior can be captured through angular margin inflation or probabilistic coverage metrics. These extensions preserve analytical tractability while improving physical fidelity. For example, one may inflate the footprint $\varsigma \to \varsigma + \Delta\varsigma$ instead of modeling, e.g., full optics or attitude jitter, where $\Delta\varsigma$ includes, attitude error, optical distortion, and refraction variability.

We now analyze the combined influence of controller performance and payload field of view (FOV) on coverage accuracy. To this end, several core concepts are first introduced. Consider a visibility cone centered at the satellite's center of mass. The intersection of the cone axis with the Earth's surface defines the ground track, while the projection of the cone onto the surface yields an ellipsoidal region representing the coverage area. We denote by $\mathcal{E}_{id}$ the ellipsoidal projection corresponding

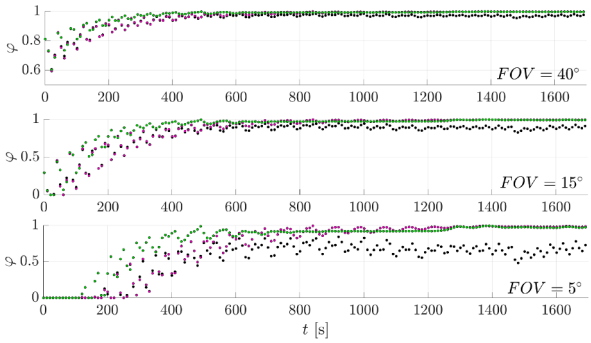

Fig. 8. Evolution of the relative misalignment between the projected area $\mathcal{E}_{id}$ of the ideal cone and the one $\mathcal{E}_R$ of the controlled cone when employing LQMPC (black), TRMPC (magenta), and OS-SMPC (green). (For interpretation of the references to colour in this figure legend, the reader is referred to the web version of this article.)

to a cone aligned with the nadir-pointing direction, and by $\mathcal{E}_R$ the ellipsoidal projection associated with the satellite actual pointing direction. Accordingly, a novel figure of merit for assessing coverage accuracy is introduced, defined as the relative overlapped area $\mathcal{A}$ between the ideal $\mathcal{E}_{id}$ and the actual $\mathcal{E}_R$ projections, i.e.,

$$\varphi(\theta_{err}, \varsigma) = \frac{\mathcal{A}\left(\mathcal{E}_R \bigcap \mathcal{E}_{id}\right)}{\mathcal{A}(\mathcal{E}_{id})},$$

which depends on pointing error θ_{err} and boresight angle ς.

In Fig. 8, the time-evolution of the metric φ is illustrated as a function of the FOV for the three control schemes. It can be seen that both the robust and stochastic schemes outperform the standard LQMPC with respect to this figure of merit, independent of the payload's FOV. Moreover, a decrease in the FOV (or equivalently θ_{cap}) is observed that amplify the effect of pointing errors on coverage accuracy. Indeed, for larger FOVs, the performance gap between the control schemes in terms of coverage accuracy is significantly reduced, with all methods achieving accuracy levels above 95%, and approaching 100% for both TRMPC and OS-SMPC.

Conversely, a smaller FOV demands more precise pointing to maintain high coverage accuracy. In this scenario, the weaker LQMPC disturbance rejection substantially compromises performance, limiting coverage area to no more than 75%. Even robust and stochastic schemes are impacted by this stringent constraint, which is reflected in their convergence behavior. OS-SMPC converges relatively quickly, whereas TRMPC requires a considerably longer time. Furthermore, while large FOV values consistently produce overlap between the ideal and actual coverage areas, smaller FOVs exhibit a transient phase at the beginning with no intersection between the desired and achieved coverage regions. We want to highlight that the initial loss of overlap observed for narrow FOV values is mainly attributable to the deliberately challenging initial conditions used in the simulations to evaluate acquisition performance. During nominal observation phases, where the spacecraft operates close to the reference attitude, such transient effects are negligible.

6. Conclusions

In this paper, a novel predictive control framework for Earth-observation satellites is introduced, addressing the critical need for high-accuracy pointing and reliable mission performance in the presence of uncertainty. By employing a novel stochastic model predictive control approach, the proposed method successfully provides probabilistic guarantees on both pointing accuracy and observation coverage, a significant advancement over conventional predictive control schemes. Moreover, the use of offline-sampling techniques to approximate chance-constrained sets proved to be a viable strategy for enabling onboard, real-time implementation, demonstrating the practicality of the solution. The simulation results confirm that the framework is capable of handling complex operational constraints and external disturbances, leading to enhanced satellite autonomy and mission reliability. Finally, the importance of aligning the performance constraints in terms of pointing error and coverage accuracy with both payload requirements and control performance is demonstrated.

CRediT authorship contribution statement

Martina Mammarella: Writing – review & editing, Writing – original draft, Visualization, Validation, Software, Methodology, Investigation, Formal analysis, Conceptualization; **Elisa Capello:** Writing – review & editing, Writing – original draft, Supervision, Methodology, Conceptualization; **Fabrizio Dabbene:** Writing – review & editing, Writing – original draft, Supervision, Methodology, Investigation, Conceptualization.

Data availability

Data will be made available on request.

Declaration of competing interest

The authors declare that they have no known competing financial interests or personal relationships that could have appeared to influence the work reported in this paper.

References

Alamo, T., Tempo, R., & Camacho, E. F. (2009). Randomized strategies for probabilistic solutions of uncertain feasibility and optimization problems. *IEEE Transactions on Automatic Control*, *54*(11), 2545–2559.

Alamo, T., Tempo, R., Luque, A., & Ramirez, D. R. (2015). Randomized methods for design of uncertain systems: sample complexity and sequential algorithms. *Automatica*, *52*, 160–172.

Ameen, T., Mukhopadhyay, S., & Qaddoumi, N. (2023). Computing robust forward invariant sets of multidimensional nonlinear systems via geometric deformation of polytopes. *IEEE Transactions on Automatic Control*, *68*(12), 8293–8300.

Bate, R. R., Mueller, D. D., White, J. E., & Saylor, W. W. (2020). Fundamentals of astrodynamics. Courier Dover Publications.

Cakaj, S., Kamo, B., Lala, A., & Rakipi, A. (2014). The coverage analysis for low earth orbiting satellites at low elevation. *International Journal of Advanced Computer Science and Applications*, *5*(6).

Currie, J., Prince-Pike, A., & Wilson, D. I. (2012). Auto-Code generation for fast embedded model predictive controllers. In *Proceedings of international conference mechatronics and machine vision in practice*.

Donati, C., Mammarella, M., & Dabbene, F. (2023). Single-state weighted particle filter with application to earth observation missions. *IFAC-PapersOnLine*, *56*(2), 6024–6029.

ECSS-E-ST-60-10C, (2008). Space engineering - Control performance. Technical Report ECSS.

Eren, U., Prach, A., Koçer, B. B., Raković, S. V., Kayacan, E., & Açıkmeşe, B. (2017). Model predictive control in aerospace systems: current state and opportunities. *Journal of Guidance, Control, and Dynamics*, *40*(7), 1541–1566.

Galuppini, G., Magni, L., & Raimondo, D. M. (2018). Model predictive control of systems with deadzone and saturation. *Control Engineering Practice*, *78*, 56–64.

Geng, X., & Xie, L. (2019). Data-driven decision making in power systems with probabilistic guarantees: Theory and applications of chance-constrained optimization. *Annual Reviews in Control*, *47*, 341–363.

Hewing, L., Kabzan, J., & Zeilinger, M. N. (2019). Cautious model predictive control using gaussian process regression. *IEEE Transactions on Control Systems Technology*, *28*(6), 2736–2743.

Hewing, L., & Zeilinger, M. N. (2018). Stochastic model predictive control for linear systems using probabilistic reachable sets. In *2018 IEEE CDC* (pp. 5182–5188).

Kerrigan, E. C. (2000). Robust constraint satisfaction: Invariant sets and predictive control. University of London.

Koller, T., Berkenkamp, F., Turchetta, M., & Krause, A. (2018). Learning-based model predictive control for safe exploration. In *2018 IEEE Conference on decision and control (CDC)* (pp. 6059–6066).

Lofberg, J. (2004). Yalmip: A toolbox for modeling and optimization in matlab. In *Computer aided control systems design, 2004 IEEE international symposium on* (pp. 284–289).

Lorenzen, M., Dabbene, F., Tempo, R., & Allgöwer, F. (2017a). Constraint-tightening and stability in stochastic model predictive control. *IEEE Transactions on Automatic Control*, *62*(7), 3165–3177.

Lorenzen, M., Dabbene, F., Tempo, R., & Allgöwer, F. (2017b). Stochastic MPC with offline uncertainty sampling. *Automatica*, *81*(1), 176–183.

Luo, W., Chu, Y.-C., & Ling, K.-V. (2005). H-Infinity inverse optimal attitude-tracking control of rigid spacecraft. *Journal of Guidance, Control, and Dynamics*, *28 (3)*, 481–494.
Mammarella, M. (2019). A Comprehensive Modeling Framework for Integrated Mission Analysis and Design of a Reusable Electric Space Tug. Politecnico di Torino.
Mammarella, M., Capello, E., Park, H., Guglieri, G., & Romano, M. (2018a). Tube-based robust model predictive control for spacecraft proximity operations in the presence of persistent disturbance. *Aerospace Science and Technology*, *77*, 585–594.
Mammarella, M., Lee, D. Y., Park, H., Capello, E., Dentis, M., & Guglieri, G. (2019). Attitude control of a small spacecraft via tube-based model predictive control. *Journal of Spacecraft and Rockets*, *56*(6), 1662–1679.
Mammarella, M., Lorenzen, M., Capello, E., Park, H., Dabbene, F., Guglieri, G., Romano, M., & Allgöwer, F. (2018b). An offline-sampling SMPC framework with application to autonomous space maneuvers. *IEEE Transactions on Control Systems Technology*, *28*(2), 388–402.
Mammarella, M., Mirasierra, V., Lorenzen, M., Alamo, T., & Dabbene, F. (2022). Chance-constrained sets approximation: A probabilistic scaling approach. *Automatica*, *137*, 110108.
Markley, F. L., & Crassidis, J. L. (2014). Fundamentals of Spacecraft Attitude Determination and Control. Springer.
Niederreiter, H. (1992). Random number generation and quasi-Monte Carlo methods (vol. 63). Siam.
Ott, T., Benoit, A., Van den Braembussche, P., & Fichter, W. (2011). Esa pointing error engineering handbook. In *8Th international ESA conference on guidance, navigation & control systems*. (*vol. 17*).
Pittelkau, M. E. (1992). Frequency weighted LQG control of spacecraft attitude. In *[proceedings 1992] The first IEEE conference on control applications* (pp. 336–341).
Prékopa, A. (1995). Stochastic Programming. Kluwer Academic Publishers.
Sun, Z., Dai, L., Liu, K., Xia, Y., & Johansson, K. H. (2018). Robust MPC for tracking constrained unicycle robots with additive disturbances. *Automatica*, *90*, 172–184.
Vidyasagar, M. (2013). Learning and Generalisation: with Applications to Neural Networks. Springer Science & Business Media.
Zhao, Q., Yu, L., Du, Z., Peng, D., Hao, P., Zhang, Y., & Gong, P. (2022). An overview of the applications of earth observation satellite data: Impacts and future trends. *Remote Sensing*, *14*(8), 1863.